RESEARCH ARTICLE

physica status solidi a
www.pss-a.com

Combined Confocal-Atomic-Force Microscope Setup for Quantum Sensing Applications with Sub-diffractional Spatial Resolution

*Sergei Trofimov and Boris Naydenov**

Quantum sensors find applications ranging from material science to biophysics. Nitrogen-vacancy (NV) center in diamond has been successfully implemented for measuring various types of signals. Optical NV center readout, routinely used in confocal microscopes, allows achieving high spatial resolution down to the diffraction limit. This work describes in detail the combined confocal-atomic-force microscope (confocal-AFM), which takes advantage of sharp AFM cantilevers, and shows its possible applications for nanoscale resolution. It demonstrates the sub-diffractional localization of NV centers with platinum-coated cantilevers and the ability to separately address optically unresolved sensors using cantilevers with ferromagnetic coating. The presented setup exhibits a lateral resolution of 13 nm, providing a tool for nanoscale quantum sensing.

1. Introduction

Quantum sensing is a rapidly developing field of research, that facilitates material science,[1] biophysics studies,[2] and investigations in fundamental physics.[3] Typical examples of quantum sensors are: superconducting qubits,[4] trapped ions,[5] and solid state defects.[6] Nitrogen-vacancy (NV) defect centers in diamond are of particular interest due to their versatility. They are routinely used as nanoscale sensors of magnetic and electric fields,[7,8] temperature,[9] pressure,[10] and rotation.[11]

The NV center consists of a substitutional nitrogen atom and an adjacent vacancy in the diamond lattice. Excited with a green (520 nm) laser, it emits photoluminescence (PL) in the red part of the visible spectrum with the zero-phonon line at 637 nm. The spin-dependent intersystem crossing gives rise to the spin-dependent PL, so that the spin state $|0\rangle$ is brighter than $|\pm1\rangle$ states (see **Figure 1**a). Therefore, it is possible to readout NV's spin state optically. In the absence of external perturbations, states $|0\rangle$ and $|\pm1\rangle$ are separated in the energy equal to an energy of a photon with the frequency of 2.87 GHz. The application of a resonant microwave (MW) field induces the transition between the spin states, resulting in a PL decrease. This effect is used in optically detected magnetic resonance (ODMR) experiments, demonstrated in Figure 1b. In the case of external magnetic field B, the resonance line in ODMR splits in two (see Figure 1c) with the splitting Δf proportional to the magnitude of the magnetic field: $\Delta f = 2\gamma B$, where $\gamma = 2.8\,\text{MHz}\,\text{G}^{-1}$ is the NV center gyromagnetic ratio. Direct current (DC) scanning magnetometry is typically performed using this effect.[12]

Although it is possible to employ single NV centers for sensing, which makes physical size of the sensor ≈1.5 Å (C—C bond length in diamond), spatial resolution in such experiments is typically limited by diffraction, since the signal is detected optically. To increase the resolution, more advanced detection techniques such as stimulated emission depletion (STED),[13] ground state depletion (GSD),[14] and photoelectrical detection can be applied.[15] Another approach consists of using atomic force microscopes (AFM) and performing scanning with diamond cantilevers or nanodiamonds containing NV centers,[12,16] cantilevers with sharp tips,[17] and ferromagnetic cantilevers to overcome the diffraction limit.[18]

This work describes a combined confocal-AFM microscope built for quantum sensing experiments taking advantage of enhanced spatial resolution offered by various AFM techniques. The performance of the setup is demonstrated with proof-of-principle experiments. Though the present article concentrates on NV centers in diamond as a test system, the utilized techniques could be applied to other luminescent centers such as defects in silicon carbide and hexagonal boron nitride.[19,20]

2. Combined Confocal-AFM Microscope

The combined confocal-AFM setup consists of a commercially available AFM device and a home-built confocal microscope for laser excitation and luminescence detection, described in detail below. Since both parts probe a sample point by point, scanning techniques are necessary to obtain AFM and PL images

---

S. Trofimov, B. Naydenov
Berlin Joint EPR Laboratory and Department Spins in Energy Conversion and Quantum Information Science (ASPIN)
Helmholtz-Zentrum Berlin für Materialien und Energie
Hahn-Meitner-Platz 1, 14109 Berlin, Germany
E-mail: boris.naydenov@helmholtz-berlin.de

The ORCID identification number(s) for the author(s) of this article can be found under https://doi.org/10.1002/pssa.202400541.

DOI: 10.1002/pssa.202400541

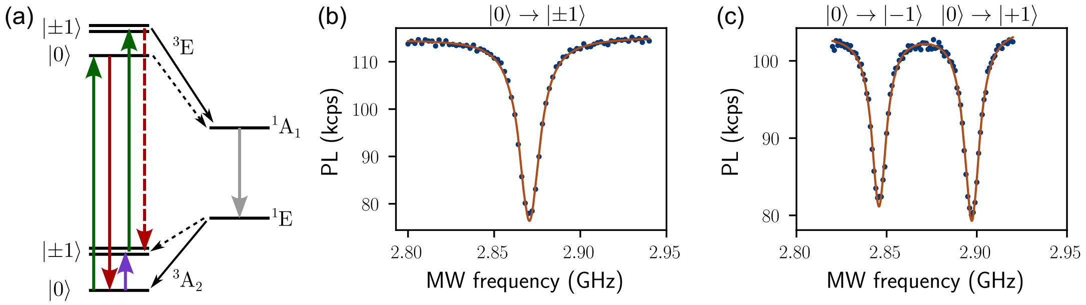

Figure 1. a) NV center energy levels. Triplet ground ($^3A_2$, GS) and excited (^3E, ES) states are split in $|0\rangle$ and $|\pm1\rangle$ spin levels. Green arrows show the laser-induced transitions between the spin states. Solid (dashed) red arrows denote the spin-dependent PL decay transitions with higher (lower) PL intensity. Solid (dashed) black arrows indicate the higher (lower) probability of intersystem crossing to and from the singlet states ($^1A_1$ and ^1E). The gray arrow denotes the infrared photon emission. The violet arrow shows the MW transition, observed in ODMR measurements; b) NV center ODMR in the absence of the magnetic field; c) NV center ODMR at magnetic field $B = 9.2$ G. ODMR data (blue points) are fitted with the Lorentzian functions (brown line).

of the sample surface. Moreover, as for typical experiments, it is necessary to bring the cantilever and the laser spot in a desired position relative to each other, an additional degree of freedom is needed. The setup described in this work is able to operate in two modes: sample scanning and laser scanning. In the former mode, the sample is moving relative to both the laser and the cantilever, while in the latter mode, the laser spot is moving relative to the sample and the cantilever. To be able to change the depth of the laser focus in the sample, the objective is also mounted on a movable piezo stage.

Another key concept of the combined setup is the control of both parts and the signal synchronization between them. The present setup uses separate control (software and hardware) of the AFM, responsible for the sample scanning, and of the confocal microscope, which is used to perform the laser scanning. The measured signals, however, are accessible by both parts in any scanning mode.

2.1. AFM Setup

The AFM microscope is an NX12 AFM manufactured by Park Systems. The device is capable of working in a wide variety of modes, the most important of which for this work are: non-contact (NC) mode and contact mode.

The combination with the confocal part is made in such a way, that while the cantilever is probing the top sample surface, the laser is focused on the same surface through the sample by the objective placed underneath as depicted in **Figure 2**a showing NV centers in diamond as an example. The AFM movable sample stage allows performing point by point sample probing (sample scanning technique), but the cantilever cannot be moved laterally. The AFM part of the setup is controlled via SmartScan software from ParkSystems.

2.2. Confocal Microscope

The confocal microscope is custom-built on the same optical table, where the AFM device is located. A schematic of the setup is shown in Figure 2b. It can be divided into three logical parts: laser preparation part, laser scanning system, and detection part. These parts are controlled via Qudi software.[21]

2.2.1. Laser Preparation Part

The sample is excited with a continuous wave (CW) green laser diode *LD* (RLT520-80MGS, Roithner LaserTechnik). An acousto-optic modulator *AOM* (AOMO 3350-199, Gooch and Housego) is used for conducting pulsed laser experiments and a single-mode

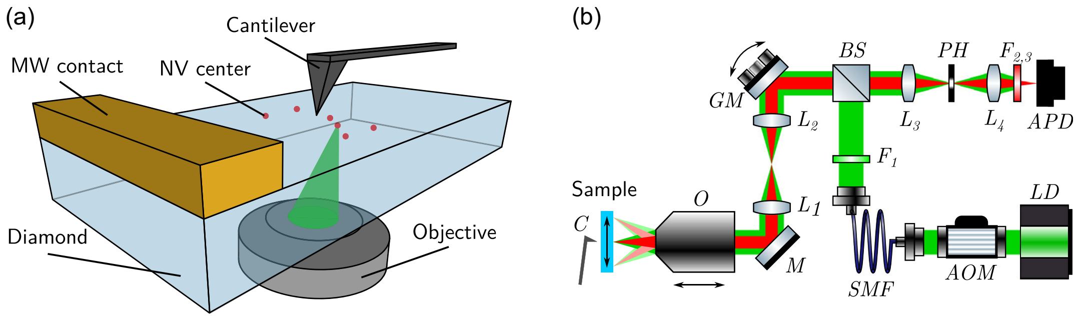

Figure 2. a) Schematic of the operating combined confocal-AFM setup; b) Schematic of the optical part of the setup. Black arrows show the sample movement during the sample scanning, galvo mirrors rotation during the laser scanning (also shown with different laser focal points), and the movement of objective for focusing. The letter abbreviations: *C*, cantilever; *O*, objective; *M*, mirror; *L*, lens; *GM*, galvo mirrors; *BS*, beam sampler; *PH*, pinhole; *F*, filter; *APD*, avalanche photodiode; *SMF*, single-mode fiber; *AOM*, acousto-optic modulator; *LD*, laser diode.

optical fiber *SMF* (P3-460P-FC-1, Thorlabs) is employed to obtain a round-shaped laser beam. After the fiber, the laser beam goes through a shortpass filter F_1 (FESH0550, Thorlabs) to remove the possible PL from the fiber, reflects from a beam sampler *BS* (SF20-B, Thorlabs), utilized to separate the excitation and detection optical paths, and enters the laser scanning system.

2.2.2. Laser Scanning System

This part is used for performing imaging with the laser scanning technique. It consists of a galvo mirror set *GM* (GVS012/M, Thorlabs), a pair of lenses L_1 and L_2 (#49-393 and #49-391, Edmund optics), and an oil objective *O* (UPLXAPO100XO, Olympus) mounted on a piezo stage (NFL5DP20S/M, Thorlabs). These objects are aligned in a 4F optical system, the operating principle of which is shown in **Figure 3** for scanning along *y*-axis.

During the scanning along y-axis, the steering angle between the laser beam and the z-axis α_y is proportional to the bias voltage V_y applied to the respective galvo mirror placed at $z = 0$, so that $\alpha_y = \frac{\partial \alpha_y}{\partial V_y} V_y$. The lens L_2 with diameter d_2 and focal distance f_2 placed at $z = f_2$ is used to make the laser beam parallel to the z-axis. The lens L_1 (d_1,f_1) placed at $z = f_1 + 2f_2$ guides the beam to the back window of the objective ($z = 2f_1 + 2f_2$) at an angle β_y, so that $\tan(\beta_y) = \frac{f_2}{f_1}\tan(\alpha_y)$. The objective *O* with focal distance f_O focuses the laser beam on the sample surface at $y_S = f_O \tan(\beta_y)$. Using $\tan(\alpha_y) \approx \alpha_y$ for small angles one readily obtains that y_S is directly proportional to the bias voltage applied to the galvo mirror

$$y_S = f_O \tan(\beta_y) = f_O \frac{f_2}{f_1} \tan(\alpha_y) \approx f_O \frac{f_2}{f_1} \alpha_y = f_O \frac{f_2}{f_1} \frac{\partial \alpha_y}{\partial V_y} V_y \tag{1}$$

From Equation (1), the scanning resolution (d*x*, d*y*) is defined by the angle resolution $d\alpha_{x,y}$. To ensure the best possible resolution of the imaging setup, it should be approximately an order of magnitude less than the diffraction limit (see Section 2.2.3). Too low d*x* and d*y* values, however, are not desirable because it means that the maximum field of view *a* can be increased (see below) without lowering the imaging resolution. For the setup described in the present work, the galvo mirror limited resolution $dx = dy \approx 32$ nm (see **Table 1**).

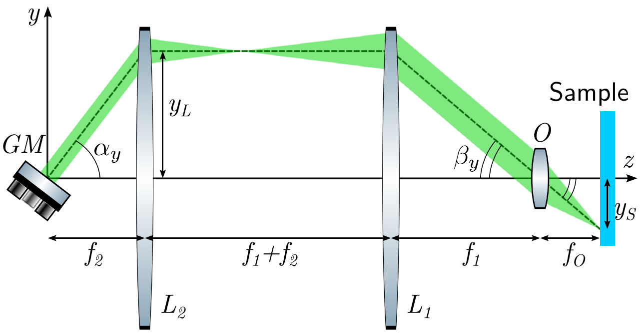

Figure 3. Operating principle of the galvo mirror scanning system. The laser beam is shown in green.

Table 1. Setup parameters.

Parameter	Value	Description
a	160 µm	Maximum field of view
$d\alpha$	30 µRad	Galvo mirror resolution
d_1	50 nm	L_1 diameter
d_2	50 nm	L_2 diameter
d_3	25 nm	L_3 diameter
d_4	25 nm	L_4 diameter
d_{las}	8 mm	Laser beam diameter before objective
d_O	7 mm	Objective back window diameter
d_p	40 µm	Pinhole diameter
f_1	250 nm	L_1 focal length
f_2	150 nm	L_2 focal length
f_3	60 nm	L_3 focal length
f_4	60 nm	L_4 focal length
f_O	1.8 mm	Objective focal length
λ_{las}	520 nm	Laser wavelength
λ_{PL}	700 nm	Average PL wavelength
NA_O	1.45	Objective numerical aperture
n	2.4	Diamond refractive index

For ideal lenses the maximum square field of view with side $a = 2x_S^{max} = 2y_S^{max}$ is limited by the diameter of the lenses d_1 and d_2 and by the diameter of the laser beam d_{las}, so that $\tan(\alpha_y^{max}) = \frac{y_L^{max}}{f_2} = \frac{d_{1,2} - d_{las}}{2\sqrt{2}f_2}$. Therefore, using Equation (1)

$$a = \frac{1}{\sqrt{2}} \frac{f_O}{f_1} (d_{1,2} - d_{las}) \tag{2}$$

Substituting the values of the parameters from Table 1 in the equation, one obtains 214 × 214 µm maximum scan size. For the current setup, however, additional limitations take place, as the galvo mirrors responsible for *x*- and *y*-axis scanning are separated by distance $\Delta_m = 15$ mm. This results in a drop of the laser intensity reaching the sample at the scan edges as shown in Supporting Information.

The laser, focused on the sample by the objective *O*, excites the studied defects at the focal point and their PL is collected via the same objective. These photons follow the excitation path to the beam sampler, where 90% of them are transmitted to the detection part of the setup.

The lateral imaging resolution of any scanning optical setup is limited by diffraction, which manifests in a finite size of the laser focal spot at the sample. This resolution limit $\delta_{x,y}$ can be calculated using the Abbe formula

$$\delta_{x,y} = 0.61 \frac{\lambda_{las}}{NA_O} \tag{3}$$

where λ_{las} is the laser wavelength, and NA_O is the numerical aperture of the objective. The axial resolution limit δ_z of such a setup can be estimated using the Rayleigh length—the length of the Gaussian laser beam profile

$$\delta_z = 2\frac{n\lambda_{\text{las}}}{(\text{NA}_O)^2} \tag{4}$$

where n is the refractive index of the sample. With the parameters from Table 1, one obtains $\delta_{x,y} \approx 220\,\text{nm}$ and $\delta_z \approx 1.2\,\mu\text{m}$.

Although this resolution allows in principle to work with single luminescent defects separated by distances larger than 1 µm, one has to consider the background PL in experiments with single-photon emitters. Indeed, the laser beam going through the sample excites luminescence which reaches the detector even from the out-of-focus planes, making working with single color centers impossible. To resolve this issue, confocal mode of microscopy is utilized, which is described in the following.

2.2.3. Detection Part

The detection part of the microscope starts after the beam sampler *BS* and consists of two lenses L_3 and L_4 (2x AC254-060-B-ML, Thorlabs), a pinhole *PH* (P40K, Thorlabs), a longpass filter F_2 (FELH0650, Thorlabs), a shortpass filter F_3 (FESH0750, Thorlabs) to filter out the AFM infrared light used for cantilever position detection, and an avalanche photodiode *APD* (SPCM-AQRH-44, Excelitas) working in a single-photon counting regime. Both lenses and the pinhole are needed for the setup to work in the confocal regime.

In this configuration, the PL collected by the objective is focused on a pinhole placed before reaching the detector. It can be shown that in the limit of an infinitesimal pinhole, the confocal microscope resolution limits improve to[22]

$$\begin{aligned} \delta_{x,y}^{\text{conf}} &\approx \frac{\delta_{x,y}}{\sqrt{2}} \\ \delta_{z}^{\text{conf}} &\approx \frac{\delta_{z}}{\sqrt{2}} \end{aligned} \tag{5}$$

From the practical point of view, however, too small pinholes are not desirable, as they decrease the PL signal.[23] Thus, for setups aimed at single-photon source imaging, the size of a pinhole is usually chosen to be equal to the characteristic size of the point spread function (PSF) at the pinhole site. For a circular lens, the lateral projection of the PSF represents the Airy pattern—a bright disk (Airy disk) with concentric rings, so the pinhole diameter is normally taken equal to the Airy disk diameter. In this case, the resolution limit is still defined by Equation (3) and (4), and the pinhole acts as a background PL filter. For the simplest microscope consisting of only one objective lens, the diameter of the Airy disk d_a can be calculated using the formula (see, e.g., [24])

$$d_a = 1.22\frac{\lambda_{\text{PL}}}{\text{NA}_O} \tag{6}$$

When working with microscopes consisting of multiple lenses, one has to account for the magnification factor. For the setup described in this work, the Airy disk diameter is defined by the following equation

$$d_a = 1.22\frac{\lambda_{\text{PL}}}{\text{NA}_O}\frac{f_1 f_3}{f_O f_2} \tag{7}$$

Substituting the values of the parameters into Equation (7), one obtains $d_a \approx 33\,\mu\text{m}$. To account for spherical and chromatic aberrations, the pinhole is chosen to be 20% larger than the Airy disk size, so that the pinhole diameter $d_p = 40\,\mu\text{m}$.

3. Operation

To demonstrate the setup capabilities, several experiments utilizing both confocal and AFM operation modes were conducted. As a test sample, we used a thin $3 \times 3 \times 50\,\mu\text{m}$ diamond plate with shallow (5–10 nm below surface) NV centers. During the experiments the NV centers are excited with the laser (300 µW of power) and their PL is collected by the confocal part of the setup. AFM techniques are used to increase the imaging resolution beyond the diffraction limit (see Section 2.2.3) and to allow separate addressing of NV centers unresolvable by optics.

3.1. Optical Resolution

The optical resolution R of a microscope can be measured by imaging point emitters. As mentioned earlier, a single NV center can be regarded as a point photon source. Therefore, it can be used to measure the PSF of the confocal microscope. Results of such measurements are shown in **Figure 4**. The PSF of a

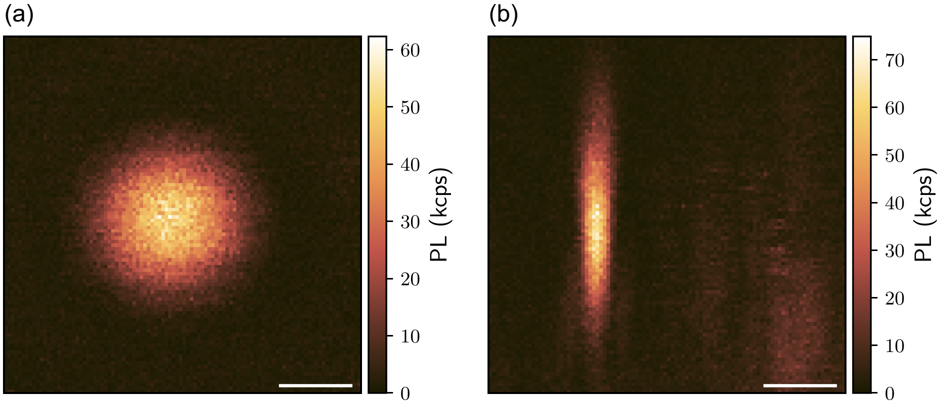

Figure 4. PL maps of a single NV center obtained via laser scanning. a) Lateral PL map PL(x, y) of a single NV center. The scale bar is 200 nm; b) Axial PL map PL(x, z) of a single NV center. The scale bar is 1 µm.

microscope consisting of a circular lens can be approximated by Gaussian functions for both lateral and axial projections.[25] In this case, the resolution is typically defined as the full width at half maximum (FWHM) of the respective Gaussian function. The lateral PSF projection shown in Figure 4a was fitted with a symmetric two-dimensional (2D) Gaussian function $G_{x,y}$, and the axial PSF projection (Figure 4b) was approximated with an asymmetric Gaussian function $G_{x,z}$, defined as

$$G_{x,y} = A_{x,y} e^{-\frac{(x-x_0)^2}{2\sigma_{x,y}} - \frac{(y-y_0)^2}{2\sigma_{x,y}}}$$
$$G_{x,z} = A_{x,z} e^{-\frac{(x-x_0)^2}{2\sigma_x} - \frac{(z-z_0)^2}{2\sigma_z}} \tag{8}$$

Using the fit parameters, the lateral resolution is found to be $R_{x,y} = 2\sqrt{2\ln 2}\sigma_{x,y} = 281 \pm 1$ nm and the axial resolution $R_z = 2\sqrt{2\ln 2}\sigma_z = 1.98 \pm 0.01$ μm. These values are larger than the ones calculated for diffraction-limited resolution $\delta_{x,y}$ and δ_z, which is attributed to the non-perfectly parallel laser beam after the L_1 and L_2 lenses and to aberrations in the PL path induced by all lenses.

3.2. Sub-diffractional NV Center Localization

AFM cantilevers were reported to modify the PL signal from NV centers, when brought in proximity to them. For example, probes with gold tips were found to enhance the NV center luminescence due to plasmonic effects at moderate tip-NV distances (>10 nm), enhancing the spatial resolution to ≈40 nm for 30 nm nanodiamonds in proximity to a ≈50 nm tip.[17] Brought at closer distances, however, a sharp metal tip induces PL quenching (see, e.g., [26]), which increases resolution of NV center imaging to ≈20 nm for sharp gold tips (<20 nm diameter).[12] Silicon cantilevers were shown to have a similar PL quenching effect stemming from a decrease in excitation and collection efficiency with resolution reaching ≈30 nm for cantilevers with the tip diameter of 20 nm.[27]

To demonstrate the setup performance, we conducted experiments aimed at the localization of NV centers with platinum coated silicon cantilevers working in contact mode (ElectriCont-G, BudgetSensors), whose effects on the NV center luminescence were not reported previously. To focus the laser at the tip position, the cantilever was engaged to the surface in the contact mode and PL imaging using the laser scanning technique at high laser power (1 mW) in the vicinity of the cantilever was conducted. As demonstrated in **Figure 5**, the tip enhances the diamond background PL from ≈8 kcounts s^{-1} (kcps) to ≈20 kcps, so it is possible to focus the laser at its position. As the cantilever tip diameter is ≈50 nm, the platinum plasmon resonance is in the near-ultraviolet (UV) spectral region,[28] so the PL enhancement is attributed to the near-filed effect.[29]

After the laser was focused at the cantilever position, the PL imaging using the sample scanning technique is conducted in the vicinity of NV centers. Results of these measurements, shown in **Figure 6**, reveal the tip-induced PL quenching of single NV centers and demonstrate the improvement of the lateral

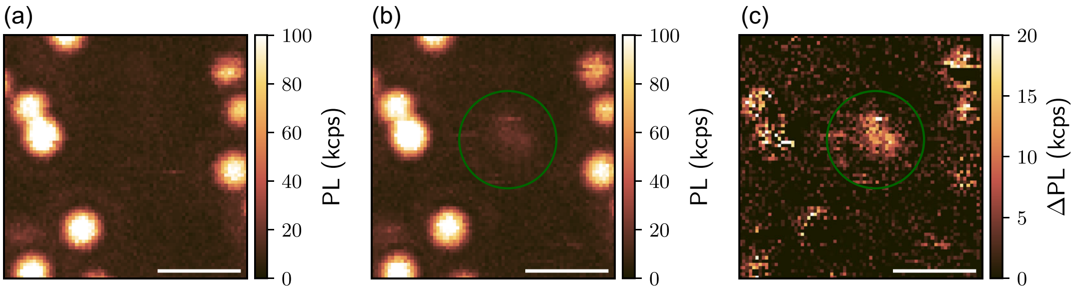

Figure 5. PL maps obtained via laser scanning. a) PL map of single NV centers with the cantilever far from the sample; b) Same image as in (a) with the cantilever in contact with the surface; c) Difference between (b) and (a). Area with cantilever-enhanced PL is circled in green. The scale bars are 1 μm.

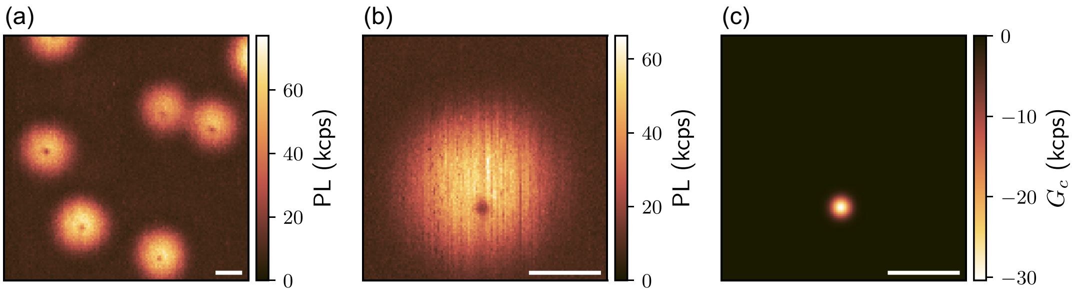

Figure 6. PL maps of single NV centers obtained via sample scanning with laser focused on the cantilever tip. a) PL map of several single NV centers; b) PL map of one NV center. The difference in the positions of the bright and the dark spots originates from an imperfect alignment of the laser focus and the cantilever tip; c) Gaussian function G_c, describing the cantilever-induced PL quenching and obtained by fitting (b) with Equation (9), shows the NV center location. The scale bars are 200 nm.

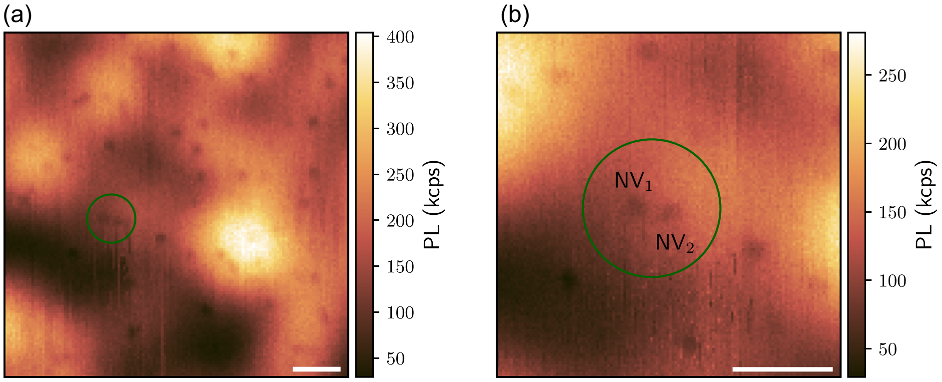

Figure 7. PL maps of optically unresolved NV centers obtained via sample scanning with laser focused on the cantilever tip. a) PL map of NV centers; b) Zoomed-in PL map showing NV$_1$ and NV$_2$ separated by 68 nm. The scale bars are 200 nm.

resolution $R_{x,y}$ to 45 ± 1 nm. Again, no NV PL increase due to plasmonic effects were detected for the platinum-coated tips.

To calculate $R_{x,y}$, the PL image of a single NV center shown in Figure 6b $\mathrm{PL}(x, y) = \mathrm{PL}(\mathbf{r})$ was fitted with a sum of two 2D Gaussian functions $G_o(\mathbf{r})$ and $G_c(\mathbf{r})$, describing the optical lateral PSF and the cantilever-assisted PL quenching respectively

$$\mathrm{PL}(\mathbf{r}) = G_o(\mathbf{r}) + G_c(\mathbf{r}) = A_o e^{-\frac{(\mathbf{r}-\mathbf{r_0})^2}{2\sigma_o}} + A_c e^{-\frac{(\mathbf{r}-\mathbf{r_c})^2}{2\sigma_c}} \tag{9}$$

The enhanced resolution is calculated as FWHM of $G_c(\mathbf{r})$: $R_{x,y} = 2\sqrt{2\ln 2}\sigma_c$.

Figure 7 shows how this approach can be used to resolve NV centers located very close to each other.

Here, a PL map is obtained in the region with a higher concentration of NV centers, so they could not be distinguished by pure optic means. The NV$_1$ and NV$_2$ circled in green in the PL map are resolved due to the PL quenching induced by the cantilever. Fitting these PL dips with Gaussian functions $G_c(\mathbf{r})$ allows to calculate the distance between them $r_{12} = 68 \pm 2$ nm.

3.3. Sub-diffractional NV Center Addressing

As mentioned previously, in nanoscale magnetometry applications the external magnetic field is probed by single NV centers, so the spatial resolution is limited by diffraction. To improve the resolution, the method described in the previous section could be used. Another approach for localization is to employ the magnetic field spatial gradient, produced by microcoils and micromagnets.[30,31] Since positioning of these objects next to NV centers is challenging, AFM probes with ferromagnetic tips could be used to produce an inhomogeneous magnetic field with a high gradient.[18,32] This gradient is also utilized to separately address optically unresolvable NV centers with the same crystallographic orientation.

To demonstrate the setup abilities, we performed NV center magnetic field imaging of a ferromagnetic cantilever. In these experiments, a magnetic probe (MagneticMulti75-G, BudgetSensors) in the NC mode was positioned next to an optically unresolvable pair of NV centers NV$_1$ and NV$_2$ shown in Figure 7b, and the laser was focused on these NVs. An ODMR spectrum taken when the cantilever is far away from the NVs is presented in **Figure** 8a. Since it shows only two resonances (compare to Figure 1c), we assume that these NV centers have the same crystallographic orientation, so they probe the same magnetic field projection. An ODMR spectrum depicted in Figure 8b shows the further splitting of the $|0\rangle \rightarrow |+1\rangle$ transition due to the magnetic field gradient, so that the NVs experience different magnetic fields $B_2 = 122$ G and $B_1 = 148$ G.

Treating the ferromagnetic tip as a magnetic dipole μ_t, oriented perpendicular to the sample surface, we assume the magnetic field dependence on the lateral distance to the tip r to be

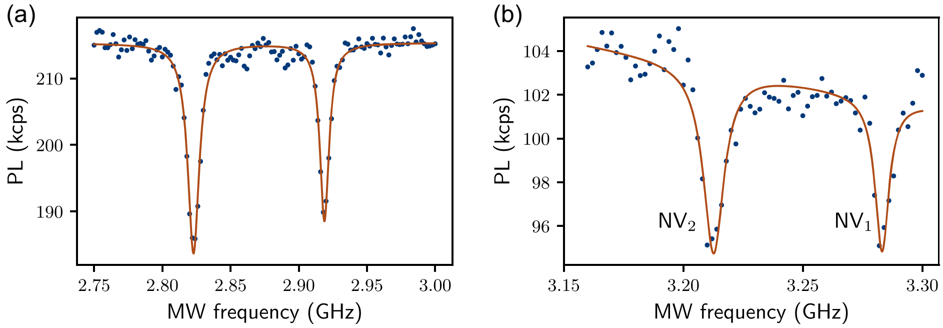

Figure 8. ODMR spectra of NV$_1$ and NV$_2$ in the presence of the ferromagnetic cantilever. a) ODMR spectrum obtained when the cantilever is far from the NVs; b) ODMR spectrum obtained when the cantilever is located close to the NVs. ODMR data (blue ponts) are fitted with a sum of two Lorentzian functions (brown line).

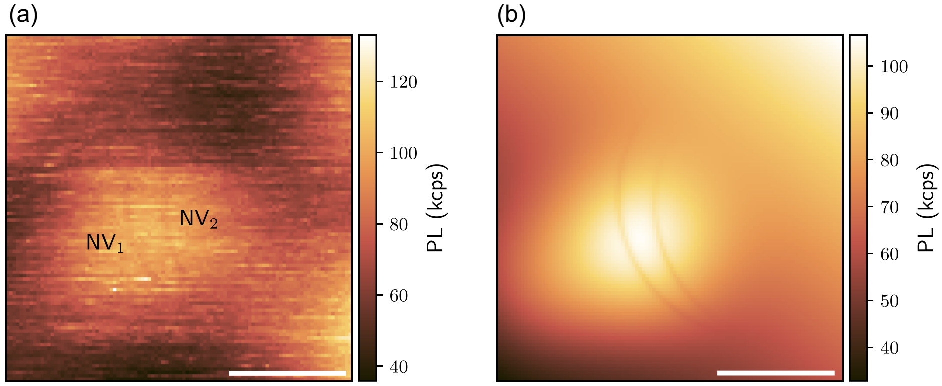

Figure 9. a) PL map obtained via sample scanning with constantly applied MWs at the frequency $f = 3.21$ GHz (NV$_2$ resonance line); b) Fit of the PL map shown in (a) as explained in the text. The scale bars are 200 nm.

$$B(r) = \frac{\mu_0}{4\pi}\frac{\mu_t}{r^3} \tag{10}$$

In this case, magnetic field lines, showing the field of constant amplitude, represent circles.

The magnetic field mapping was performed using sample scanning at constantly applied microwaves at the NV$_2$ resonance frequency $f = 3.21$ GHz. During the scanning process, both NV centers move in the vicinity of the tip, experiencing different magnetic fields due to the high gradient. The PL map shown in **Figure 9**a contains the bright spot indicating the NV center position crossed over by two dark circular lines. Since the MWs are applied at the fixed frequency, each of the NV center is in the magnetic resonance with the certain magnetic field $B = 122$ G. When any of these NVs crosses the corresponding magnetic field line, the NV PL intensity decreases. Thus, each dark line in the map corresponds to same magnetic field line of the cantilever probed by two optically unresolvable NV centers NV$_1$ and NV$_2$ as indicated in Figure 9a.

To fit each of the two NVs in the obtained PL map, we used a 2D Gaussian function $G_o(\mathbf{r})$ overlapped with a Lorentzian-shaped 2D ring $L_c(\mathbf{r})$

$$\begin{aligned}\mathrm{PL}(\mathbf{r}) &= G_o(\mathbf{r}) \cdot [1 + L_c(\mathbf{r})] \\ &= A_o e^{-\frac{(\mathbf{r}-\mathbf{r_o})^2}{2\sigma_o}} \left[1 + A_c \frac{\gamma_c^2}{(|\mathbf{r} - \mathbf{r_c}| - R)^2 + \gamma_c^2}\right]\end{aligned} \tag{11}$$

For both of the NV centers the parameter R, representing the radius of the magnetic field line, was kept the same. From the fit, shown in Figure 9b, one derives the distance between the NV centers as the distance between the centers of the dark rings $r_{1,2} = |\mathbf{r}_{c,1} - \mathbf{r}_{c,2}| = 65 \pm 29$ nm, which agrees well with the value obtained using the tip-induced quenching technique (see Section 3.2). The large uncertainty of the determined distance stems from the fact, that in this experiment we detect only a part of these dark rings, which results in a comparatively large uncertainties of the positions of their origins. The spatial resolution $R_{x,y}$ can be calculated as the FWHM of the dark rings (FWHM $= 2\gamma_c$), and for the map shown in Figure 9a $R_{x,y} = 13 \pm 3$ nm. The spatial resolution can be further improved by bringing the ferromagnetic cantilever closer to the NV centers, which leads to an increase in the magnetic field gradient. At very high gradients, however, acoustic noise and vibrations that introduce uncertainties in the cantilever position result in unstable ODMR lines. Therefore, to further improve the spatial resolution, it is necessary to apply sophisticated noise-cancelling techniques. The radius of the probed magnetic field line was found to be $R = 243 \pm 22$ nm. Using the distance between NV centers $r_{1,2}$ and the difference in magnetic field that they experience, calculated from ODMR spectrum, we find the tip gradient to be $\nabla_r B = \frac{B_1 - B_2}{r_{1,2}} = 0.4 \pm 0.2$ G nm^{-1}. Using Equation (10), one can estimate the magnetic dipole moment of the cantilever to be $\mu_t = 2 \times 10^{-12}$ emu.

4. Conclusion

The present work describes a combined confocal-AFM microscope and its applications for sub-diffraction localization of luminescent defects and for NV center-based magnetometry. The setup demonstrates ≈10 nm resolution in PL imaging of shallow NV centers in diamond and shows the ability to separately address NV centers unresolvable with optical means. The results indicate that in contrast to gold cantilevers, platinum tips of the same diameter do not exhibit a significant plasmon-related PL enhancement, while still inducing a PL quenching at the lateral NV-tip distances comparable to the tip diameter. This nanoscale localization can be utilized to determine the position of single NV centers in diamond nanopillars with high precision, which is crucial for the scanning NV magnetometry.[12] Finally, the available electrical AFM modes of the setup, which are not employed this work, could be used in the same setup configuration for photoelectrical detection of defects in solids with sub-micron spatial resolution.[33]

Supporting Information

Supporting Information is available from the Wiley Online Library or from the author.

Acknowledgements

The authors are grateful to Alexander Klasen, Andrea Cerreta, Florian Stumpf, and Ilka Hermes from Park Systems for the experimental support.

The authors acknowledge Park Systems for the financial support. They also thank Oleg Dogadov for fruitful discussions. This work was supported by German Research Foundation (DFG, grant nos. 410866378 and 410866565) and by German Federal Ministry of Education and Research (BMBF, grant no. 16KISQ034K).

Open Access funding enabled and organized by Projekt DEAL.

Conflict of Interest

The authors declare no conflict of interest.

Data Availability Statement

The data that support the findings of this study are available from the corresponding author upon reasonable request.

Keywords

AFM, NV center, sub-diffractional resolution

Received: July 1, 2024
Revised: July 29, 2024
Published online: September 4, 2024

---

[1] F. Casola, T. Van Der Sar, A. Yacoby, *Nat. Rev. Mater.* **2018**, *3*, 17088.
[2] M. A. Taylor, W. P. Bowen, *Phys. Rep.* **2016**, *615*, 1.
[3] D. F. Jackson Kimball, D. Budker, T. E. Chupp, A. A. Geraci, S. Kolkowitz, J. T. Singh, A. O. Sushkov, *Phys. Rev. A* **2023**, *108*, 010101.
[4] R. Kleiner, D. Koelle, F. Ludwig, J. Clarke, *Proc. IEEE* **2004**, *92*, 1534.
[5] M. Brownnutt, M. Kumph, P. Rabl, R. Blatt, *Rev. Modern Phys.* **2015**, *87*, 1419.
[6] D. D. Awschalom, R. Hanson, J. Wrachtrup, B. B. Zhou, *Nat. Photonics* **2018**, *12*, 516.
[7] J. M. Taylor, P. Cappellaro, L. Childress, L. Jiang, D. Budker, P. R. Hemmer, A. Yacoby, R. Walsworth, M. D. Lukin, *Nat. Phys.* **2008**, *4*, 810.
[8] F. Dolde, H. Fedder, M. W. Doherty, T. Nöbauer, F. Rempp, G. Balasubramanian, T. Wolf, F. Reinhard, L. C. L. Hollenberg, F. Jelezko, J. Wrachtrup, *Nat. Phys.* **2011**, *7*, 459.
[9] P. Neumann, I. Jakobi, F. Dolde, C. Burk, R. Reuter, G. Waldherr, J. Honert, T. Wolf, A. Brunner, J. H. Shim, D. Suter, H. Sumiya, J. Isoya, J. Wrachtrup, *Nano Lett.* **2013**, *13*, 2738.
[10] M. W. Doherty, V. V. Struzhkin, D. A. Simpson, L. P. McGuinness, Y. Meng, A. Stacey, T. J. Karle, R. J. Hemley, N. B. Manson, L. C. Hollenberg, S. Prawer, *Phys. Rev. Lett.* **2014**, *112*, 047601.
[11] A. A. Wood, E. Lilette, Y. Y. Fein, N. Tomek, L. P. McGuinness, L. C. L. Hollenberg, R. E. Scholten, A. M. Martin, *Sci. Adv.* **2018**, *4*, eaar7691.
[12] P. Maletinsky, S. Hong, M. S. Grinolds, B. Hausmann, M. D. Lukin, R. L. Walsworth, M. Loncar, A. Yacoby, *Nat. Nanotechnol.* **2012**, *7*, 320.
[13] E. Rittweger, K. Y. Han, S. E. Irvine, C. Eggeling, S. W. Hell, *Nat. Photonics* **2009**, *3*, 144.
[14] E. Rittweger, D. Wildanger, S. W. Hell, *Europhys. Lett.* **2009**, *86*, 14001.
[15] P. Siyushev, M. Nesladek, E. Bourgeois, M. Gulka, J. Hruby, T. Yamamoto, M. Trupke, T. Teraji, J. Isoya, F. Jelezko, *Science* **2019**, *363*, 728.
[16] L. Rondin, J.-P. Tetienne, P. Spinicelli, C. Dal Savio, K. Karrai, G. Dantelle, A. Thiaville, S. Rohart, J.-F. Roch, V. Jacques, *Appl. Phys. Lett.* **2012**, *100*, 153118.
[17] Y. Yung Hui, Y.-C. Lu, L.-J. Su, C.-Y. Fang, J.-H. Hsu, H.-C. Chang, *Appl. Phys. Lett.* **2013**, *102*, 013102.
[18] M. S. Grinolds, P. Maletinsky, S. Hong, M. D. Lukin, R. L. Walsworth, A. Yacoby, *Nat. Phys.* **2011**, *7*, 687.
[19] M. Widmann, S.-Y. Lee, T. Rendler, N. T. Son, H. Fedder, S. Paik, L.-P. Yang, N. Zhao, S. Yang, I. Booker, A. Denisenko, M. Jamali, S. A. Momenzadeh, I. Gerhardt, T. Ohshima, A. Gali, E. Janzén, J. Wrachtrup, *Nat. Mater.* **2015**, *14*, 164.
[20] A. Gottscholl, M. Kianinia, V. Soltamov, S. Orlinskii, G. Mamin, C. Bradac, C. Kasper, K. Krambrock, A. Sperlich, M. Toth, I. Aharonovich, V. Dyakonov, *Nat. Mater.* **2020**, *19*, 540.
[21] J. M. Binder, A. Stark, N. Tomek, J. Scheuer, F. Frank, K. D. Jahnke, C. Müller, S. Schmitt, M. H. Metsch, T. Unden, T. Gehring, A. Huck, U. L. Andersen, L. J. Rogers, F. Jelezko, *SoftwareX* **2017**, *6*, 85.
[22] T. Wilson, *J. Microsc.* **2011**, *244*, 113.
[23] C. J. R. Sheppard, M. Castello, G. Tortarolo, A. Zunino, E. Slenders, P. Bianchini, G. Vicidomini, A. Diaspro, *J. Opt. Soc. Am. A* **2023**, *40*, 138.
[24] E. Hecht, in *Optics*, Addison-Wesley, San Francisco, CA **2002**.
[25] B. Zhang, J. Zerubia, J.-C. Olivo-Marin, *Appl. Opt.* **2007**, *46*, 1819.
[26] F. M. Huang, F. Festy, D. Richards, *Appl. Phys. Lett.* **2005**, *87*, 183101.
[27] X. Ye, M. Wang, P. Wang, R. Li, M. Guo, P. Yu, H. Liu, F. Shi, Y. Wang, J. Du, *J. Phys. Photonics* **2021**, *3*, 014003.
[28] S. Jung, K. L. Shuford, S. Park, *J. Phys. Chem. C* **2011**, *115*, 19049.
[29] J. M. Gerton, L. A. Wade, G. A. Lessard, Z. Ma, S. R. Quake, *Phys. Rev. Lett.* **2004**, *93*, 180801.
[30] K. Arai, C. Belthangady, H. Zhang, N. Bar-Gill, S. J. DeVience, P. Cappellaro, A. Yacoby, R. L. Walsworth, *Nat. Nanotechnol.* **2015**, *10*, 859.
[31] N. Sadzak, M. Héritier, O. Benson, *Sci. Rep.* **2018**, *8*, 8430.
[32] G. Balasubramanian, I. Y. Chan, R. Kolesov, M. Al-Hmoud, J. Tisler, C. Shin, C. Kim, A. Wojcik, P. R. Hemmer, A. Krueger, T. Hanke, A. Leitenstorfer, R. Bratschitsch, F. Jelezko, J. Wrachtrup, *Nature* **2008**, *455*, 648.
[33] K. Klein, B. Hauer, B. Stoib, M. Trautwein, S. Matich, H. Huebl, O. Astakhov, F. Finger, R. Bittl, M. Stutzmann, M. S. Brandt, *Rev. Sci. Instrum.* **2013**, *84*, 103911.